Near-Wall Convection in a Sedimenting Suspension of Fibers

Feng Zhang and Anders A. Dahlkild
Linné FLOW Centre, KTH Mechanics, Royal Institute of Technology, 100 44 Stockholm, Sweden

Katarina Gustavsson
Linné FLOW Centre, KTH Mathematics, Royal Institute of Technology, 100 44 Stockholm, Sweden

Fredrik Lundell
Linné FLOW Centre, KTH Mechanics, Royal Institute of Technology, 100 44 Stockholm, Sweden

Wallenberg Wood Science Centre, KTH Mechanics, Royal Institute of Technology, 100 44 Stockholm, Sweden

DOI 10.1002/aic.14576
Published online August 21, 2014 in Wiley Online Library (wileyonlinelibrary.com)

The sedimentation of a fiber suspension near a vertical wall is investigated numerically. Initially, the near-wall convection is an upward backflow, which originates from the combined effects of the steric-depleted layer and a hydrodynamically depleted region near the wall. The formation of the hydrodynamically depleted region is elucidated by a convection-diffusion investigation, in which fibers are classified according to the different directions in which they drift. For fibers with sufficiently large aspect ratio, the initial near-wall backflow keeps growing. However, the backflow reverses to downward flow at later times if the aspect ratio is small. This is due to the fiber-wall interactions which rotate fibers to such angles that make fibers drift away from the wall, inducing a dense region and a correspondingly downward flow outside the initial backflow. Moreover, the steric-depleted boundary condition is of secondary importance in the generation and evolution of the near-wall convection. © 2014 American Institute of Chemical Engineers
AIChE J, 60: 4253–4265, 2014
Keywords: fibers, fluid mechanics, settling/sedimentation, multiphase flow

Introduction

When studying the dependence of the sedimentation velocity of sphere suspensions on the shape of the container in the dilute regime, Mazur and his coworkers[1–3] found that the relative sedimentation velocity is indeed container-shape independent. However, there exists a convection of the suspension in which the fluid and particles move together. This global convection phenomenon, which does depend on the container shape, has been called intrinsic convection. Bruneau et al.[4] used a simple model to show that this convection originates in the buoyancy of the particle-depleted layers next to the sidewalls. Their model considers a cell with vertical walls and a sedimenting suspension of point-force spheres distributed uniformly in the cell. The spheres are allowed to overlap with one another but not with the wall. Thus, the centers of the spheres cannot come closer to the wall than one particle radius. As a result, a buoyant particle-depleted layer can drive an upward flow near the wall, which drags the bulk of suspension up with it. The circulation is completed by a downward return flow in the center. Bruneau et al.[5] also extended the model to the three-dimensional (3-D) case. An experimental investigation[6] has confirmed the existence of a global intrinsic convection of the suspension superimposed on the settling motion of the particles. However, the effect was much smaller than predicted and even disappeared with increasing concentrations.

To our knowledge, this phenomenon has not been investigated in nonspherical particle suspensions. When studying the concentration fluctuations in sedimentation of orientable particle suspensions, Saintillan et al.[7] in their simulation model found upward flow at the vertical walls, where a tangential flow boundary condition was applied. However, they simply attributed this to the particle-depleted layers. Nevertheless, in the current article, this near-wall backflow is studied in detail by an Eulerian method. The advective fiber motion is obtained by the slender body approximation complemented with the method of images. We will propose a different mechanism leading to near-wall particle depletion essentially independent of steric depletion for nonspherical particle suspensions.

However, when adopting an Eulerian approach, for example, Ref. 8, it is not a trivial matter to capture the unique, near-wall behavior of fiber suspensions. The simplest and most easily applied wall boundary condition for the probability density function is a simple no-flux condition. However, for anisotropic particles, the no-flux condition requires some thought. For example, if the center of a fiber is positioned at a distance less than $l/2$ (l is the fiber length) away from a wall, the fiber is not free to rotate into any orientation as some configurations place one end of the fiber inside the wall. Figure 1b illustrates this by showing the closest possible approach of a fiber center to the two walls of a plane channel for different orientation angles. Thus, the existence

Correspondence concerning this article should be addressed to A. A. Dahlkild at ad@mech.kth.se.

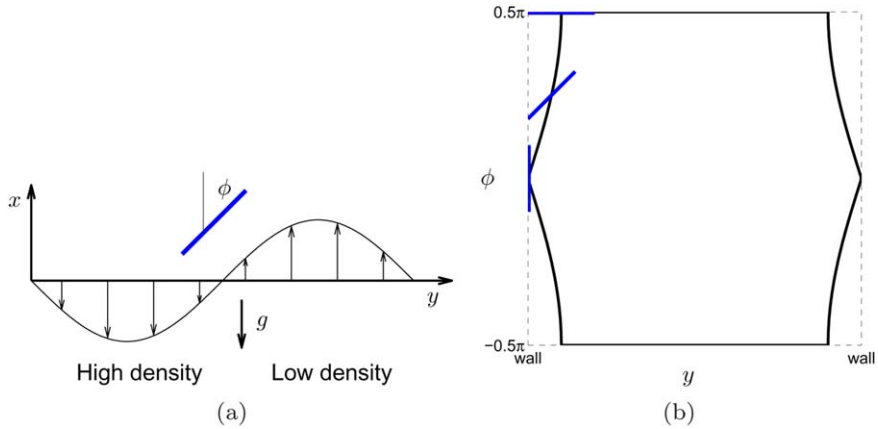

Figure 1. Sketch of the studied vertical planar motion and the computational domain.

(a) Definition of coordinate system, orientation angle, and sketch of velocity profile as generated by density differences in the suspension. (b) Computational domain. The curved lines indicate the closest possible position of a fiber center to the left and right wall, respectively, for different orientation angles. Three fibers just touching the left wall are displayed by blue lines at angles $\phi=0,\pi/4,\pi/2$. [Color figure can be viewed in the online issue, which is available at wileyonlinelibrary.com.]

of a set of forbidden orientation states close to each wall is required. The basis for this condition lies in the impenetrability of a rigid particle through a solid wall. Nitsche and Brenner[9] and Nitsche[10] presented a general framework for the construction of the near-wall boundary conditions based on the impenetrability condition. Schiek and Shaqfeh[11] implemented these boundary conditions and showed that the surface over which the no-flux boundary condition must be satisfied is a complex hypersurface that forbids any part of the fiber from penetrating the wall. These hypersurface near-wall boundary conditions were also used by Krochak et al.[12]

In the Stokesian limit, a prolate or oblate particle drifts laterally at intermediate orientations without rotation in an unbounded fluid. However, when it approaches a wall, the interaction with the wall will induce rotational motions. According to the theoretical analysis of Caswell,[13] as a particle approaches the sidewall at small angles, the leading end of the particle rotates away from the wall (negative angular velocity), and it turns through the vertical and drifts away. Although at larger angles, the wall causes the particle to pivot and then drift away. These two kinds of motions are termed as "glancing" turn and "reversing" turn, respectively.[14] The "glancing" turn was observed by de Mestre[15] experimentally. de Mestre and Russel[16] theoretically presented the drag and induced torque on a slender cylinder translating parallel with or normal to a single plane wall. The direction and rate of rotation were given for those cases which also indicate the "glancing" and "reversing" turns. Russel et al.[14] derived the motion of an inertialess rod-like object falling near a flat wall in Stokes flow. They found that the rod performs the two kinds of motions near the wall depending on the initial orientations. They concluded that between two parallel plates, the rod undergoes a periodic motion. Experiments and numerical solution confirming the theoretical analysis were also performed. Particle settling in a tube is also investigated in a Stokes flow.[17,18] In studying shear-driven and pressure-driven flow, Schiek and Shaqfeh[11] argued that when the separation distance of a fiber and wall is larger than $l/2$, the translational velocity of the fiber is not affected by the wall. When the distance is less than $l/2$, only the horizontal translational velocity is weakly changed based on the experiments of Russel et al.[14] Thus, it is reasonable to neglect the change of the hydrodynamic mobility of a fiber as it approaches a wall. Moreover, this approximation was also adopted by Krochak et al.[12] when they investigated a fiber suspension in a plane channel flow. According to the comparison between their experimental data and the model predictions, they found a good agreement particularly near the channel walls. However, in the current study on sedimenting fiber suspensions, the wall-induced particle motions will be included.

In this work, we present novel mechanisms for the convection next to the sidewall in an initially quiescent and well-mixed suspension. This article is organized as follows: the methods are described in section Methods, where the steric-depleted boundary condition is introduced in detail. Additionally, the slender body approximation together with the method of images are used to calculate the wall-induced motions of a fiber. The results for different aspect ratios are presented in section Results, followed by conclusions in the last section.

Methods

Motions of mixture and fibers

A dilute fiber suspension is described by the distribution function $\Psi(\boldsymbol{p},\boldsymbol{x},t)$ denoting the normalized number density of particles at position $\boldsymbol{x}$ with fiber orientation vector $\boldsymbol{p}$. The time evolution of $\Psi(\boldsymbol{p},\boldsymbol{x},t)$ is governed by the Fokker–Planck equation

$$\frac{\partial}{\partial t}\Psi(\boldsymbol{p},\boldsymbol{x},t)+\nabla_p\cdot\boldsymbol{F}_p+\nabla_x\cdot\boldsymbol{F}_x=0 \tag{1}$$

where the flux densities $\boldsymbol{F}_x$ and $\boldsymbol{F}_p$ are defined by

$$\boldsymbol{F}_p=\dot{\boldsymbol{p}}(\boldsymbol{p},\boldsymbol{x},t)\Psi(\boldsymbol{p},\boldsymbol{x},t)-\mathbf{D_p}\cdot\nabla_p\Psi(\boldsymbol{p},\boldsymbol{x},t) \tag{2}$$

$$\boldsymbol{F}_x=\dot{\boldsymbol{x}}(\boldsymbol{p},\boldsymbol{x},t)\Psi(\boldsymbol{p},\boldsymbol{x},t)-\mathbf{D_x}\cdot\nabla_x\Psi(\boldsymbol{p},\boldsymbol{x},t) \tag{3}$$

and where ∇_p is the gradient operator in orientation space. $\mathbf{D_p}$ and $\mathbf{D_x}$ correspond to rotational diffusion and translational diffusion of fibers, respectively. $\dot{\boldsymbol{p}}$ is the rotational velocity of a spheroid. $\dot{\boldsymbol{x}}$ is the linear velocity of a particle at position $\boldsymbol{x}$ which can be considered as the sum of the sedimentation velocity of the particle $\boldsymbol{v}_s(\boldsymbol{p})$ with orientation vector $\boldsymbol{p}$ in a quiescent, pure fluid, and the fluid disturbance velocity $\boldsymbol{u}(\boldsymbol{x},t)$ at position $\boldsymbol{x}$.[19] Conservation of momentum and volume require

$$\rho(\alpha)\left(\frac{\partial \boldsymbol{u}}{\partial t}+\boldsymbol{u}\cdot\nabla\boldsymbol{u}\right)=-\nabla P+(\rho(\alpha)-\rho_0)\boldsymbol{g}+\mu_e\nabla^2\boldsymbol{u} \quad (4)$$

$$\nabla\cdot\boldsymbol{u}=0 \quad (5)$$

where

$$\rho(\alpha)=\alpha\rho_{\mathrm{p}}+(1-\alpha)\rho_{\mathrm{f}} \quad (6)$$

is the local density of the dilute suspension, ρ_{f} fluid density, ρ_{p} particle density, and $\alpha(\boldsymbol{x},t)$ the local volume fraction of the particles whose average value is $\alpha_0 \ll 1$. Here, we have introduced the reduced pressure $P=p-\rho_0\boldsymbol{g}\cdot\boldsymbol{x}$, where p is the pressure and ρ_0 is the average suspension density. The effective viscosity μ_e is simply taken as constant $\mu=\nu\rho_0$ due to the dilute limit.

In the present work, a vertical, columnar planar motion of the fluid is considered, see Figure 1a. Thus, the disturbance is assumed to be a planar horizontal wave as introduced by the presence of the planar vertical wall. Following Zhang et al.,[20] we take the fibers to be oriented in one and the same plane, that is, the x-y plane, which is an additional simplification of the problem. This was motivated by Zhang et al.[20] through their stability analysis for plane orientation in an infinite suspension, which qualitatively gave the same result for growth rates as that obtained by Dahlkild[8] using the full 3-D orientation state of the fibers in a plane wave. Thus, there is reason to believe that the present results obtained from the assumption of a planar orientation state are at least qualitatively correct.

The single orientational dimension is chosen as the angle ϕ between the fiber major axis and the gravity direction. The horizontal coordinate y is the only nonhomogeneous spatial dimension. Thus, in the dilute limit and periodic domain, the rotational motion[21] and horizontal component of the linear velocity see Ref. 8 for details of the particles are, respectively

$$\dot{\phi}_p=\frac{1}{2}\left(\frac{r^2-1}{r^2+1}\cos 2\phi-1\right)\frac{\partial u}{\partial y} \quad (7)$$

$$\dot{y}_p=-\frac{F_{\mathrm{g}}}{8\pi\mu a}[\ln(2r)-1.5]\sin 2\phi \quad (8)$$

where r is the aspect ratio of the fibers and a is half fiber length. Here, the gravity force $F_{\mathrm{g}}=\Delta\rho g V$ where $\Delta\rho$ is the density difference of the fibers and the surrounding fluid, g is the gravitational acceleration, $V=\pi l^3/6r^2$ is the volume of one fiber.

The active components of the diffusivity tensors are $D_{\phi\phi}$ and D_{yy}. Here, we choose the same diffusivities as Zhang et al.[20]

$$D_{yy}=C_{yy}aV_{\mathrm{s}}, D_{\phi\phi}=C_{\phi\phi}\dot{\gamma}\frac{\alpha_0 r}{\ln^2 r} \quad (9)$$

where $a=l/2$ is half the fiber length, V_{s} the settling velocity of a vertical isolated fiber

$$V_{\mathrm{s}}=\frac{F_{\mathrm{g}}}{8\pi\mu a}[2\ln(2r)-1] \quad (10)$$

and $\dot{\gamma}$ the magnitude of the shear rate, that is, $|\partial u/\partial y|$. The parameters are chosen as $C_{yy}=0.3$ and $C_{\phi\phi}=0.3$. For more details, we refer to Zhang et al.[20]

Steric-depleted boundary condition

Because the fibers are symmetric, the ends of a fiber are indistinguishable. Thus, periodic boundary conditions are specified in the orientational dimension ϕ, that is

$$\Psi(\phi,y,t)=\Psi(\phi+\pi,y,t) \quad (11)$$

$$\frac{\partial\Psi}{\partial\phi}(\phi,y,t)=\frac{\partial\Psi}{\partial\phi}(\phi+\pi,y,t) \quad (12)$$

We consider the orientation angles on half the unit circle with $\phi\in[-\pi/2,\pi/2]$. Note that the fiber angle is defined positive, $\phi>0$, if it orients as shown in Figure 1.

Boundary conditions in the horizontal y-direction are imposed by two vertical walls at a distance W apart. Due to the impenetrability of the solid walls, we must have

$$\boldsymbol{n}\cdot\boldsymbol{F}=n_\phi F_\phi+n_y F_y=0 \quad (13)$$

where $\boldsymbol{n}$ is the local normal to the wall surfaces in y–ϕ space (see Figure 1b) separating the allowed and forbidden fiber orientation states and $\boldsymbol{F}$ is the flux density of the fibers. $\boldsymbol{n}$ is expressed as follows

$$\boldsymbol{n}_{\mathrm{L}}=\begin{cases}-a\cos\phi\boldsymbol{e}_\phi+\boldsymbol{e}_y, & 0\le\phi\le\pi/2\\ a\cos\phi\boldsymbol{e}_\phi+\boldsymbol{e}_y, & -\pi/2\le\phi\le 0\end{cases} \quad (14)$$

on the left side wall, $y=-\frac{W}{2}+a\sin|\phi|$, and

$$\boldsymbol{n}_{\mathrm{R}}=\begin{cases}-a\cos\phi\boldsymbol{e}_\phi-\boldsymbol{e}_y, & 0\le\phi\le\pi/2\\ a\cos\phi\boldsymbol{e}_\phi-\boldsymbol{e}_y, & -\pi/2\le\phi\le 0\end{cases} \quad (15)$$

on the right side wall, $y=\frac{W}{2}-a\sin|\phi|$. The flux density components are

$$F_\phi=\dot{\phi}\Psi-D_{\phi\phi}\frac{\partial\Psi}{\partial\phi} \quad (16)$$

$$F_y=\dot{y}\Psi-D_{yy}\frac{\partial\Psi}{\partial y} \quad (17)$$

In principle, the normal component of a single fiber's rotational and translational advective motion must be canceled at the hypersurface, that is, $n_\phi\dot{\phi}+n_y\dot{y}=0$. However, for slender fibers, this close to wall-interaction would appear in a thin boundary layer at the hypersurface of the order of the fiber diameter in thickness. The slender body approximation presented in the next sub-section to model the influence of the wall on the fiber motion is not accurate enough to deal with the lubrication layer that appears as the fiber's end point comes close to the wall. Our hypothesis here is that this layer is of secondary importance as one considers a suspension of many fibers subjected also to hydrodynamic interactions between fibers. These interactions are modeled by the diffusion fluxes of translation and rotation. Thus, any advective flux of fibers that places one end of the fiber through the wall, due to the deficiency of the near-wall treatment, is balanced here by a diffusive flux in the opposite direction. The present model also neglects any additional tangential flux taking place in the innermost boundary layer close to the hypersurface. This should be justified as long as the diffusive layer is substantially thicker.

Equation 13 states that any rotational flux that places one end of the fiber into the walls must be balanced by a translation flux that moves the center of the fiber away from the walls. Alternatively, any translational flux that places one end of the fiber into the walls must be balanced by a rotational flux that orients the fiber closer to the vertical direction. Note that these boundary conditions alone do not necessarily include hydrodynamic interactions with the walls, but rather consider the steric depletion of allowable

orientation states only. In addition to the periodicity and no-flux requirements, the normalization constraint is

$$\frac{1}{W}\int_{-W/2}^{W/2}\frac{1}{\pi}\int_{\phi_2}^{\phi_1}\Psi(\phi,y,t)d\phi dy=1 \tag{18}$$

where W is the distance between the sidewalls and functions ϕ_1 and ϕ_2 refer to the minimum and maximum allowed angles in the ϕ direction for a given y position. For the geometry shown in Figure 1b, ϕ_1 and ϕ_2 are defined as

$$\phi_1=\begin{cases}\pi/2, & |y|\le(W/2-a)\\ \arcsin(y/a+W/l), & y\le(a-W/2)\\ \arcsin(W/l-y/a), & y\ge(W/2-a)\end{cases} \tag{19}$$

and $\phi_2=-\phi_1$. Thus, the particle flux in the y–ϕ plane can only be tangential to these hypersurfaces. Hereafter, this kind of boundary condition is referred to as steric-depleted boundary condition. A less detailed account of the wall would just require zero translational flux and neglect the steric depletion of orientation states. This is referred to as the no-flux boundary condition and is obtained if ϕ_1 is defined as $\phi_1=\pi/2$ for all y.

Wall influence on a sedimenting fiber

To take into account the influence of a wall on a sedimenting fiber, the slender body approximation together with the method of images will be used. The basic idea behind the slender body approximation is to approximate the representation of the effect of a fiber on the fluid by a distribution of singularities along its axis.[22] A nonlocal slender body approximation can be derived by placing Stokeslets and doublets on the fiber centerline, then applying the technique of matched asymptotic to derive the approximate equation. The formulation is closed by enforcing a no-slip condition on the fiber surface, assuming the velocity to be a function of arc-length only. In this derivation, higher order terms in $\varepsilon=1/2r\ll 1$ have been neglected, and the accuracy of the final equation for the velocity of the fiber centerline is of order $O(\varepsilon^2\ln\varepsilon)$. We will refer to ε as the slenderness parameter. For details on the derivation, see the work of Keller and Rubinow,[23] Johnson,[24] and Götz.[25] The derivation yields an integral equation with a modified Stokeslet kernel on the fiber centerline and relates the fiber forces to the velocity of the centerline. The formulation includes the nonlocal interaction of the fiber with itself, as mediated by the surrounding fluid. For a detailed description of this approach applied to many interacting fibers, see Tornberg and Gustavsson[26]; Gustavsson and Tornberg.[27]

The most common way of including a plane wall is to use the method of images.[28] The idea is that an image fiber, reflected in the wall, is added to the system and an additional set of singularities along the image fiber are applied in such fashion that the resulting velocity field fulfills the zero velocity condition at the wall.

At a given time, denote the coordinates of the centerline of a fiber as $\boldsymbol{X}(s)=\boldsymbol{x}_c+s\boldsymbol{p}$, where $\boldsymbol{x}_c$ denotes the center coordinate and s denotes a coordinate along the fiber centerline. We will work with a nondimensional form of the formulation such that $-1\le s\le 1$, which means that the characteristic length is chosen to be the half-length of the fiber, a. As characteristic velocity and time scales, we use V_s and $t_s=a/V_s$.

The nondimensional form of the equation for the velocity of the centerline of a fiber is then given by

$$\begin{aligned}\kappa(\dot{\boldsymbol{x}}_c+s\dot{\boldsymbol{p}})=&[\kappa(\mathbf{I}+\boldsymbol{pp})+2(\mathbf{I}-\boldsymbol{pp})]\cdot\boldsymbol{f}(s)\\&+(\mathbf{I}+\boldsymbol{pp})\cdot\boldsymbol{K}[\boldsymbol{f}](s)+\boldsymbol{V}^W(s)\end{aligned} \tag{20}$$

where $\boldsymbol{f}$ is the force distribution on the fiber exerted by the fluid. The constant $\kappa=-\ln(\varepsilon^2 e)$. In all these expressions, $\boldsymbol{pp}$ is a dyadic product, that is, $(\boldsymbol{pp})_{ij}=(\boldsymbol{p})_i(\boldsymbol{p})_j$. The integral operator $\boldsymbol{K}[\boldsymbol{f}](s)$, is given by

$$\boldsymbol{K}[\boldsymbol{f}](s)=\int_{-1}^{1}\frac{\boldsymbol{f}(s')-\boldsymbol{f}(s)}{|s'-s|}ds' \tag{21}$$

Finally, $\boldsymbol{V}^W$ in (20) takes into account the interaction between the fiber and the wall and is given by

$$\boldsymbol{V}^W(s)=\int_{-1}^{1}\mathbf{G}^W(\boldsymbol{R})\cdot\boldsymbol{f}(s')ds' \tag{22}$$

with $\boldsymbol{R}(s,s')=\boldsymbol{X}(s)-\boldsymbol{X}^{IM}(s')$ where $\boldsymbol{X}(s)$ is a point on the fiber and $\boldsymbol{X}^{IM}(s')$ is a point on the image fiber. $\mathbf{G}^W$ is the Green's function for a flow bounded by a plane wall located at $y=0$ and is in our case given by

$$\mathbf{G}^W(\boldsymbol{R})=-\mathbf{S}(\boldsymbol{R})+2h^2\mathbf{G}^D(\boldsymbol{R})-2h\mathbf{G}^{SD}(\boldsymbol{R}) \tag{23}$$

where

$$S_{ij}(\boldsymbol{x})=\frac{\delta_{ij}}{|\boldsymbol{x}|}+\frac{x_ix_j}{|\boldsymbol{x}|^3}$$

$$G^D_{ij}(\boldsymbol{x})=\pm\frac{\partial}{\partial x_j}\left(\frac{x_i}{|\boldsymbol{x}|^3}\right)=\pm\left(\frac{\delta_{ij}}{|\boldsymbol{x}|^3}-3\frac{x_jx_j}{|\boldsymbol{x}|^5}\right)$$

$$G^{SD}_{ij}(\boldsymbol{x})=\pm\frac{\partial S_{i2}}{\partial x_j}=x_2G^D_{ij}(\boldsymbol{x})\pm\frac{\delta_{j2}x_i-\delta_{i2}x_j}{|\boldsymbol{x}|^5}$$

with a minus sign for $j=2$ corresponding to the y-direction and a plus sign for $j=1$, 3, corresponding to the x- and z-directions.[28,29] The distance in the y-direction between a point on the fiber and the wall is denoted by h.

The unknowns in (20) are the translational and rotational velocities, $\dot{\boldsymbol{x}}_c$ and $\dot{\boldsymbol{p}}$, and the force distribution along the fiber $\boldsymbol{f}(s)$. To close the formulation, we use the fact that the fibers are rigid, that is, they must perform a rigid body rotation and the total force and torque on the fiber must balance the external forces applied to the system

$$\int_{-1}^{1}\boldsymbol{f}(s)ds=\boldsymbol{F},\quad \int_{-1}^{1}s\boldsymbol{p}\times\boldsymbol{f}(s)ds=\boldsymbol{M} \tag{24}$$

Here, $\boldsymbol{F}$ is given by the gravitational force with a magnitude equal to one (due to the nondimensionalization) and the external torque, $\boldsymbol{M}$, will be equal to zero.

Instead of discretizing and solving (20) and (24) directly, we expand the force distribution as a sum of $N+1$ Legendre polynomials, $P_n(s)$

$$\boldsymbol{f}=\frac{1}{2}\boldsymbol{F}+\sum_{n=1}^{N}\boldsymbol{a}^nP_n(s) \tag{25}$$

where the coefficients $\boldsymbol{a}^n$ are unknown vectors with three components, one for each direction in space. The choice of N will be a parameter in the numerical algorithm. With this approach, the coefficients $\boldsymbol{a}^n$, will be given as the solution to a linear system of equations derived from (20) and (24) using the force expansion (25), orthogonality properties of the Legendre polynomials and the fact that the

operator $\boldsymbol{K}$ in (20) diagonalizes under the Legendre polynomials.[25]

The system of equations to be solved for the coefficients, $\boldsymbol{a}^n$, will be of size $3N\times 3N$ and is

$$\boldsymbol{a}^1+D_1\boldsymbol{pp}\cdot\sum_{k=1}^{N}\Theta^{k1}\cdot\boldsymbol{a}^k=-\frac{1}{2}D_1\boldsymbol{pp}\cdot\Theta^{01}\cdot\boldsymbol{F} \tag{26}$$

$$\boldsymbol{a}^n+\gamma_n(\mathbf{I}-E_n\boldsymbol{pp})\cdot\sum_{k=1}^{N}\Theta^{kn}\cdot\boldsymbol{a}^k=-\frac{1}{2}\gamma_n(\mathbf{I}-E_n\boldsymbol{pp})\cdot\Theta^{0n}\cdot\boldsymbol{F} \tag{27}$$

with the second equation for $n=2,\ldots,N$. Here

$$\gamma_n=(2n+1)/[2(2+\kappa-\lambda_n)],\quad D_1=\frac{3}{4(\kappa-\lambda_1)},\quad E_n=\frac{\kappa-2-\lambda_n}{2(\kappa-\lambda_n)}$$

where $\lambda_n=2\sum_{i=1}^{n}(1/i)$. The 3×3 matrix Θ^{kn} is defined as

$$\Theta^{kn}=\int_{-1}^{1}\left[\int_{-1}^{1}\mathbf{G}^W(\boldsymbol{R})P_k(s')ds'\right]P_n(s)ds$$

with $\mathbf{G}^W$ as defined in (23). For full details, see Tornberg and Gustavsson.[26]

Once the system of equation for the Legendre coefficients has been solved, the force distribution can be computed using (25) and the translational and rotational velocities can then be computed according to

$$\dot{\boldsymbol{x}}_c=\frac{1}{2\kappa}[\kappa(\mathbf{I}+\boldsymbol{pp})+2(\mathbf{I}-\boldsymbol{pp})]\cdot\boldsymbol{F}+\frac{1}{2\kappa}\int_{-1}^{1}\boldsymbol{V}^W(s)ds \tag{28}$$

$$\dot{\boldsymbol{p}}=\frac{3}{2\kappa}(\mathbf{I}-\boldsymbol{pp})\cdot\int_{-1}^{1}s\boldsymbol{V}^W(s)ds \tag{29}$$

All occurring integrals are evaluated numerically by splitting the integration interval into N_q subintervals, using a three-point Gauss quadrature on each interval.

Numerical implementation

A commercial code, COMSOL multiphysics, is used in our simulations to obtain the simultaneous solution of the coupled Fokker–Planck and Navier–Stokes equations with computational domains shown in Figure 1. Equations 28 and 29 are solved via a MATLAB package code to get the wall-induced translational velocity $\dot{y}_w$ and rotational velocity $\dot{\phi}_w$ in the x-y plane. Thus, the total rotational velocity $\dot{\phi}$ and total translational velocity $\dot{y}$ of the particles become, respectively

$$\dot{\phi}=\dot{\phi}_p+\dot{\phi}_w,\dot{y}=\dot{y}_p+\dot{y}_w \tag{30}$$

In the present article, the Reynolds number $Re=lV_s\rho/\mu$ is 10^{-3}, the crowding number $N_c=\alpha_0 r^2$ is 0.5 and the separation distance $W=100a$. Hereafter, the translational velocities of particles and disturbance bulk velocities are nondimensionalized by V_s. Rotational velocities of particles and time t are nondimensionalized by $t_s=a/V_s$. The distance to the wall y is nondimensionalized by a. The wall on the left side is located at $y=0$.

Results

In this section, the near-wall configurations are investigated in detail. The mechanisms of the generation of the near-wall concentration disturbance and the corresponding near-wall convection are explained by a convection-diffusion analysis. The effects of changing the magnitude of the translational diffusivity and also the aspect ratio of the fibers are studied. In the end, we show that the effects of the steric-depleted boundary condition are of secondary importance.

Wall-induced motions of a falling fiber

When a fiber settles near a plane wall, de Mestre and Russel[16] presented the equations for the rotational motions for $\phi=0$ and $\pi/2$, respectively

$$\dot{\phi}_0=-\frac{3}{2\ln(2r)-1}\left[\frac{y^2+1/2}{(1+1/y^2)^{1/2}}-y^2\right] \tag{31}$$

$$\dot{\phi}_1=\frac{3}{8\ln(2r)-4}\left[1+(y^2-1)\ln\left(1-\frac{1}{y^2}\right)\right] \tag{32}$$

Note that $(\dot{\phi}_0,\dot{\phi}_1)\sim\frac{f(y)}{2\ln(2r)-1}$. Thus, if the aspect ratio of the fiber is smaller, the absolute values of $\dot{\phi}_0$ and $\dot{\phi}_1$ are increased. For aspect ratio $r=10$, the numerical results $\dot{\phi}_w$ from (29) are plotted in Figure 2 together with results from (31) and (32). It shows that these two results are identical.

In the y–ϕ phase field, the wall-induced rotational velocity $\dot{\phi}_w$ and translational velocity $\dot{y}_w$ are calculated and displayed in Figure 3. Here, ϕ is scaled by π. For $-0.5<\phi<0$, $\dot{\phi}_w$ is symmetric around $\phi=0$ whereas $\dot{y}_w$ is antisymmetric. In the simulations, the results of $\dot{\phi}_w$ and $\dot{y}_w$ are interpolated on the grid points linearly.

Large aspect ratio: r = 30

Using steric-depleted boundary condition and including the wall-induced motions ($\dot{\phi}_w$ and $\dot{y}_w$), the first case is calculated with aspect ratio $r=30$. To illustrate the effects of the sidewalls, we show a partial region near the left wall at different times in Figure 4. The suspension is homogeneous and isotropic in the phase field at $t=0$, that is, $\Psi(\phi,y,0)=1$ and $u(y,0)=0$. It shows the evolution of Ψ, u (scaled by V_s) and the local concentration perturbation of the particles α'. Here, the local volume fraction $\alpha(y)$ is defined as

$$\alpha(y,t)=\frac{\alpha_0}{\pi}\int_{\phi_2}^{\phi_1}\Psi(\phi,y,t)d\phi \tag{33}$$

and the perturbation is defined as $\alpha'=\alpha/\alpha_0-1$. Note that although Ψ is a constant at $t=0$, the volume fraction close to the wall is not a constant, due to the steric depletion of fibers. Thus, the initial volume fraction changes from zero, at $y=0$, to α_0, at $y=1$, in the steric depletion layer. Initially, particles settle sideways according to their orientations, for example, fibers with positive angles drift to the left side wall as shown in Figure 4a. Thus, strong F_y can be observed and one also can see the accumulation of fibers with $\phi>0$ and the absence of fibers with $\phi<0$ near the wall in the Ψ plot. In parallel with the velocity plot, the dash-dot line shows the distribution of the volume fraction of the fibers. In the vicinity of the steric-depleted layer adjacent to the wall, there is a narrow fiber-rich layer due to the fibers with positive angles that accumulate near the wall. However, outside this fiber-rich layer, there is a wider depletion region which is due to the strong absence of fibers with negative angles. Accordingly, an upward flow is driven near the wall, which in fact induces a weak downward flow in the center. In Figure 4b, the large shear rate in the backflow adjacent to the wall causes a negative orientational flux of the fibers, as indicated by the arrows, which makes the fibers orient themselves closer to $\phi=0$ and also move closer to the wall. Thus, as the particles are more aligned with the wall,

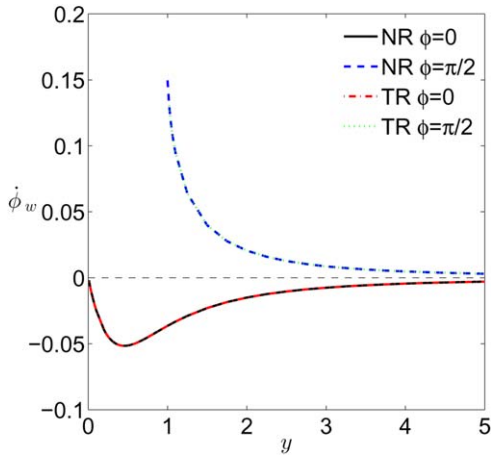

Figure 2. Wall-induced rotational velocities, $\dot{\phi}_w$ for aspect ratio $r = 10$; NR: Numerical results; TR: Theoretical results from (31) and (32).

The distance to the wall y is nondimensionalized by a. The wall on the left side is located at $y = 0$. [Color figure can be viewed in the online issue, which is available at wileyonlinelibrary.com.]

the steric-depleted layer is thinner. Note that the near-wall backflow grows continuously with time and the rotational motions of the particles are dominated by the shear. As a result, strong F_ϕ is obtained. At time $t = 50$ in Figure 4c, the fibers are almost vertically aligned and the deviation from the vertical is due to the rotational diffusion.[20]

In all, Figure 4 illustrates that the suspension experiences an instability as a result of an interaction with the wall. It is initiated by an asymmetric accumulation/depletion of fibers with positive/negative angles at the wall but with minor change of the volume fraction. Subsequently, the nonlinear advection of particles produce enhanced changes in volume fraction. The associated shear rate of the flow that is set up, then enforces the instability in a manner similar to the instability in an unbounded domain. (In an unbounded domain, an initially uniform suspension becomes inhomogeneous and the fibers tend to align in the direction of gravity and clump together to form streamers.) For a more detailed description on the concentration instability, we recommend the review by Guazzelli and Hinch.[30] To illustrate the major mechanisms of the generation of the near-wall configurations, some simplified cases will be presented next.

In Figure 5a, a closeup of Figure 4a is displayed near the wall. There are two areas (indicated I and II) where α is smaller than average. Moreover, the outer hydrodynamically depleted region (II) is wider than the near-wall steric-depleted layer (I) but the amplitude of the depletion is smaller. To demonstrate which area causes the backflow, we formulate a simplified case (shown in Figure 5b) with no-flux boundary condition which neglects the steric-depleted layer. In other words, we assume that the fibers can penetrate the wall until the centers of mass of the fibers reach the wall. The wall-induced motions ($\dot{\phi}_w$ and $\dot{y}_w$) are adjusted to fit the geometry as well. Except from the fact that the immediate near-wall volume fraction distribution is different from the original case (Figure 5a), the results from the second case in Figure 5b are qualitatively quite similar. Results at later times are not shown here, but are qualitatively identical to what we have shown in Figure 4. In the simplified case, backflow is still generated near the wall, where the hydrodynamically depleted region appears outside a narrow fiber-rich layer next to the wall. Thus, the effects of the steric-depleted boundary condition on the evolution of the suspension are quite minor, and the near-wall backflow is generated even without the steric depletion of the fibers close to the wall. Note that the steric-depleted layer still has some contribution to the backflow, but is the primary contributor only in the very beginning. This is explained in the next sub-section. Another simplification is considered by excluding the wall-induced motions. The results are shown in Figures 5c, d, applying the steric-depleted boundary condition and the simplified no-flux boundary condition, respectively. Comparing Figures 5a, b with 5c, d, one finds that in this case of large aspect ratio, $r = 30$, the wall-induced motions do not change the overall pattern. The hydrodynamically depleted region in Figures 5c, d is slightly wider and larger in magnitude and makes a larger contribution to the upward flux. Therefore, the overall effect of the wall appears insensitive to the details of the choice of boundary condition and near-wall modeling of the fiber motion. Then, the question is how the hydrodynamically depleted region is created. The results from Figure 5c are adopted to do the following analysis.

In a quiescent suspension, fibers just settle according to their orientation and also diffuse when concentration gradients appear.

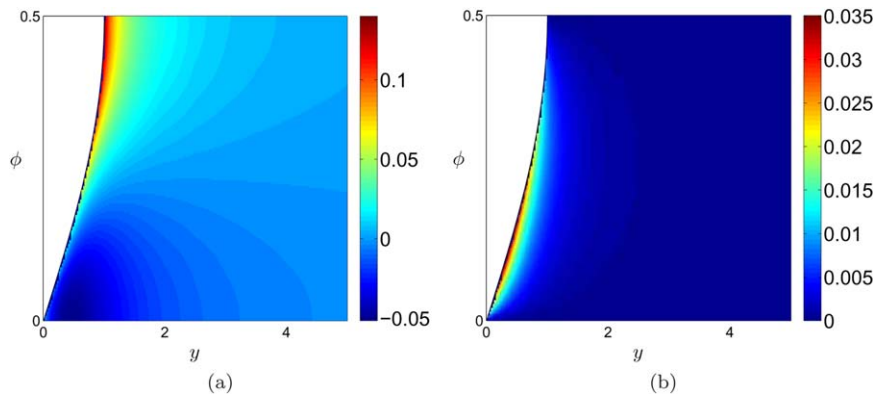

Figure 3. Single fibre's wall-induced velocities for aspect ratio $r = 10$.

(a) Wall-induced rotational velocity, $\dot{\phi}_w$ and (b) wall-induced translational velocity $\dot{y}_w$ of a single fiber settling near a plane wall in y–ϕ phase space. Here, ϕ is scaled by π. [Color figure can be viewed in the online issue, which is available at wileyonlinelibrary.com.]

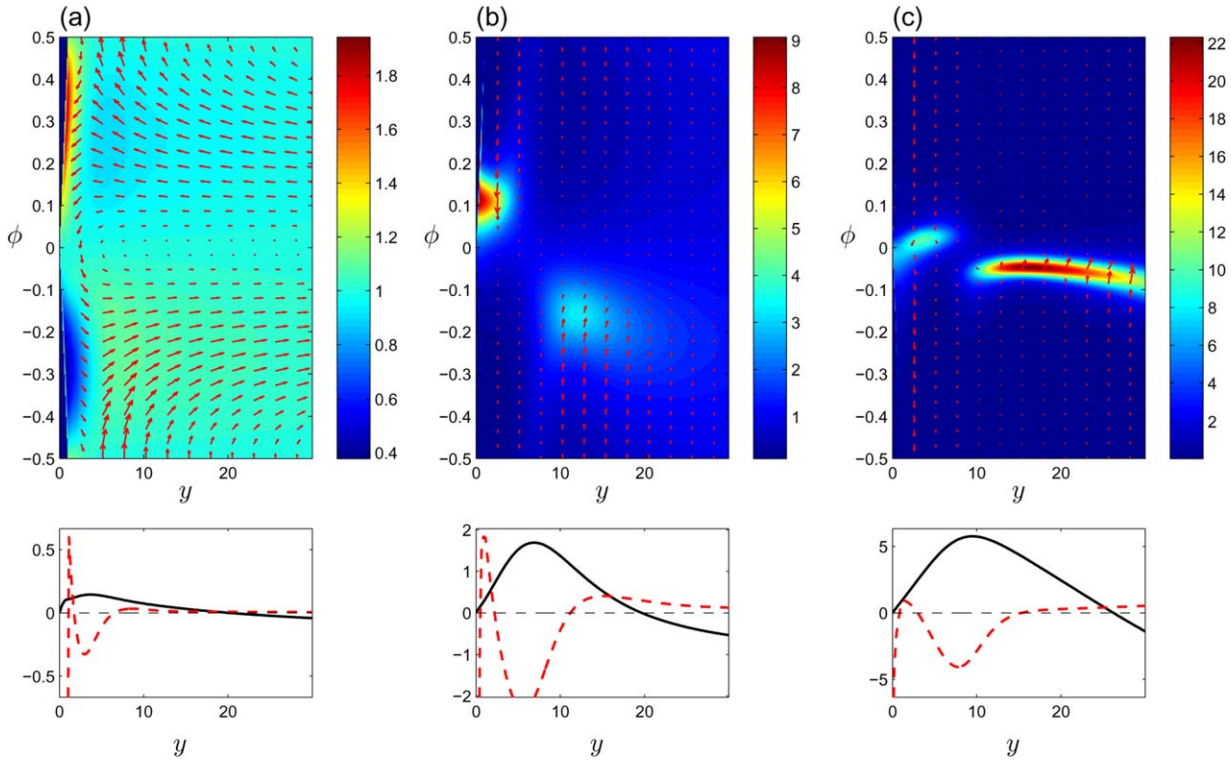

Figure 4. Aspect ratio $r = 30$.

Contour plot of $\Psi(y, \phi, t)$ (top). Velocity profile $u(y, t)$ (solid line) and particle concentration perturbation profile $10\alpha'$ (the dash-dot line) (bottom) at $t = 10$, 30, and 50 from (a) to (c). Arrows indicate the direction of the flux density vector (F_y, F_ϕ). [Color figure can be viewed in the online issue, which is available at wileyonlinelibrary.com.]

Thus, this problem can be considered a convection-diffusion problem. At early times, say, we may neglect the small fluid velocity and shear rate. Fibers are classified according to their orientation angles, that is, in which direction they drift. For fibers with $\phi > 0$ which settle toward the left wall, the convective and diffusive fluxes shown in Figure 6a are defined as

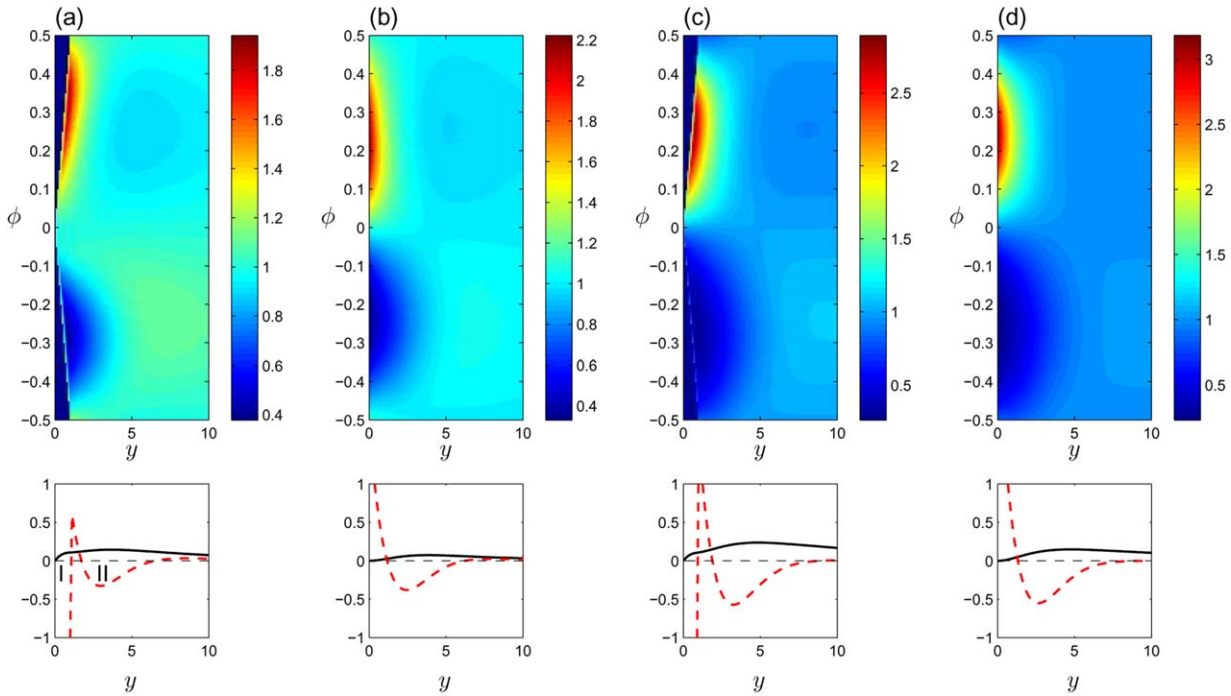

Figure 5. Aspect ratio $r = 30$.

Contour plot of $\Psi(y, \phi, t)$ (top). Velocity profile $u(y, t)$ (solid line) and particle concentration perturbation profile $10\alpha'$ (the dash-dot line) (bottom) at $t = 10$ for different cases. Four cases: (a) steric-depleted boundary condition and wall-induced motions; (b) no-flux boundary condition and wall-induced motions; (c) steric-depleted boundary condition and no wall-induced motions; (d) no-flux boundary condition and no wall-induced motions. In (a), the two depleted regions are marked I and II. [Color figure can be viewed in the online issue, which is available at wileyonlinelibrary.com.]

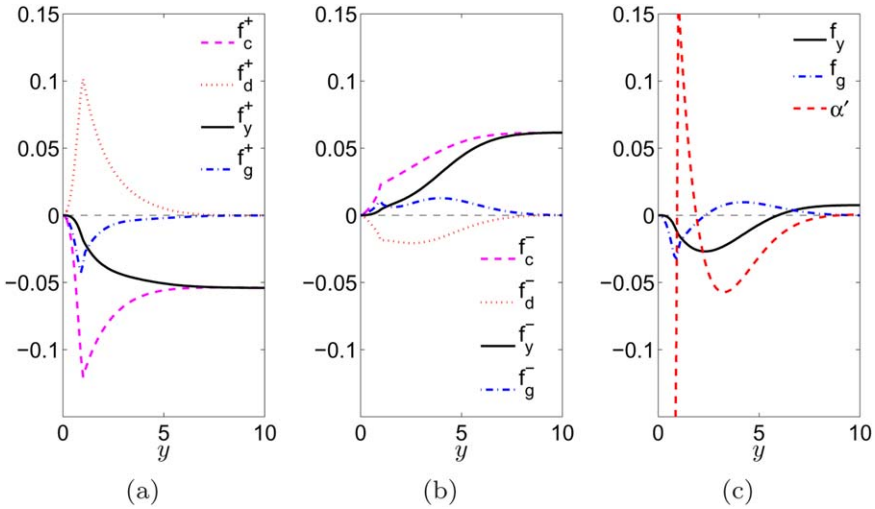

Figure 6. Aspect ratio $r = 30$ and at $t = 10$.

(a) Fluxes of fibers with $\phi>0$. f_c^+: convective flux; f_d^+: diffusive flux; f_y^+: total flux; f_g^+: spatial gradient of f_y^+. (b) Fluxes of fibers with $\phi<0$. (c) f_y: total flux of all fibers; f_g: spatial gradient of f_y; α': concentration perturbation. Negative fluxes are toward the wall. [Color figure can be viewed in the online issue, which is available at wileyonlinelibrary.com.]

$$f_c^+ = \frac{1}{\pi}\int_0^{\phi_1} \dot{y}\Psi d\phi,\ f_d^+ = -\frac{1}{\pi}\int_0^{\phi_1} D_{yy}\frac{\partial \Psi}{\partial y} d\phi \qquad (34)$$

and $f_y^+ = f_c^+ + f_d^+$. f_g^+ is the spatial gradient of f_y^+. The corresponding variables for fibers with $\phi < 0$ are displayed in Figure 6b. The total flux, $f_y = f_y^+ + f_y^-$, and its spatial gradient, f_g, are plotted in Figure 6c together with α'. In Figure 6, all the flux variables are scaled by V_s. As shown in Figures 5c and 6a, fibers with $\phi > 0$ settle toward the wall (giving a negative convective flux f_c^+) and accumulate near the wall (inducing a positive diffusive flux f_d^+). Note that these two kinds of fluxes have opposite directions. Also, due to the existence of the impenetrable wall, they result in a thin convection-diffusion layer. For fibers settling away from the wall ($\phi < 0$) shown in Figure 6b, the two kinds of fluxes also have different directions but the convection here is away from the wall. They result in a wider convection-diffusion layer. Thus, the accumulation of fibers going toward the wall will dominate in a narrow region next to the wall, whereas the depletion of fibers departing from the wall will dominate further away from the wall.

In fact, the rate of change of the volume fraction can also be obtained from the gradients of the fluxes, for example, negative flux gradient increases the volume fraction. If one compares the range and magnitude of f_g^+ and f_g^-, one can see that the magnitude of f_g^+ in Figure 6a is larger than that of f_g^- in Figure 6b but the range of influence is smaller and limited to the region nearest the wall. The combined effects of them are displayed in Figure 6c via f_g. The concentration, α', is strongly increased in a narrow region near the wall where f_g is negative. On the contrary, the decrease of the concentration further away from the wall is relatively weaker but appears in a wider region where f_g is positive. This confirms the conclusions we give based on convection-diffusion layers previously.

For this convection-diffusion problem, one would expect the behavior to be different with various translational diffusivities. Thus, we present some cases calculated with different translational diffusivities ($C_{yy}=0.03, 0.3$) and also with no-flux boundary condition and steric-depleted boundary condition, respectively. The rotational diffusivities are still the same as in other cases, $C_{\phi\phi}=0.3$. The backflow is observed near the wall regardless of the chosen values of translational diffusivities and boundary conditions. Here, the concentration distributions and velocities from the cases with steric-depleted boundary condition are given in Figure 7. At an early time $t = 10$, Figure 7a shows that increasing the diffusivity, α is changed with less magnitude but in a wider region of influence due to the nature of diffusion. For the case with smaller C_{yy}, the deficit of the fibers is more limited near the wall. Correspondingly, the peak of the velocity is closer to the wall. However, at a later time $t = 50$ shown in Figure 7b, the near-wall backflow is highly reduced, compared to the case with larger C_{yy}. With time increasing, the near-wall backflow will eventually disappear. One can also expect that the weak near-wall backflow could vanish if C_{yy} is even smaller. Instead, a near-wall downward flow can be observed. However, when the wall-induced motions are not included, the backflow near the wall is always obtained regardless of the diffusivities. Thus, the reason of the reversion of the near-wall convection is related to the wall-induced motions, which will be studied in more detail in the next section.

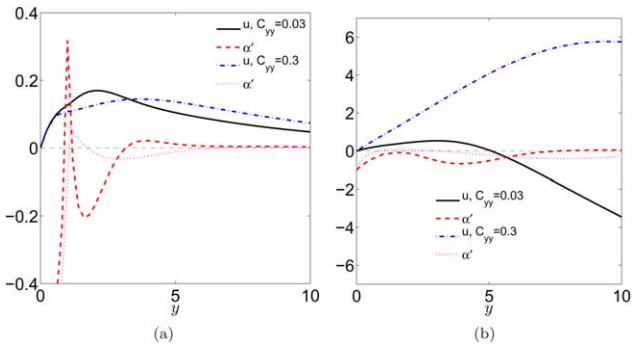

Figure 7. Aspect ratio $r = 30$ and at time (a) $t = 10$ and (b) 50.

Concentration perturbation distributions α' and disturbance velocity profiles u, with steric-depleted boundary condition and different translational diffusivities, C_{yy}. [Color figure can be viewed in the online issue, which is available at wileyonlinelibrary.com.]

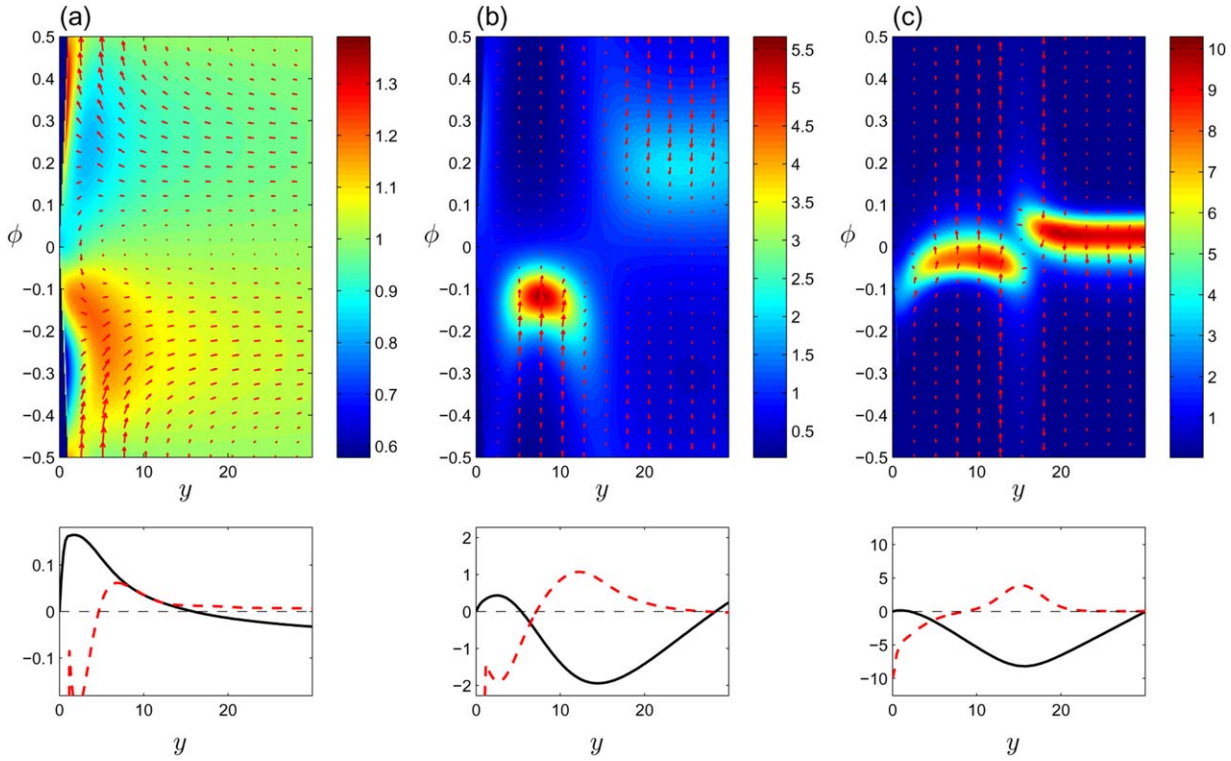

Figure 8. As for Figure 4 but with aspect ratio $r = 10$.

[Color figure can be viewed in the online issue, which is available at wileyonlinelibrary.com.]

Moderate aspect ratio: r = 10

Another case is carried out with aspect ratio $r = 10$ while the other parameters and conditions are the same as those of Figure 4. The results are shown in Figure 8. At $t = 10$, a near-wall backflow is created also in this case, alike the results in Figure 4a. However, the near wall positive peak of the volume fraction disturbance is absent, and instead there is an accumulation of fibers outside and adjacent to a near-wall-depleted region. Correspondingly, a strong downward flow is generated in this extended densified region. As a result, the near-wall convection is depressed at $t = 30$ (Figure 8b) and it reverses to a downward flow at $t = 50$ in Figure 8c. The cases shown in Figure 5 were reconsidered but now with $r = 10$. It was observed that the steric-depleted boundary condition still has negligible effects on the evolution (not shown).

For the same case but without wall-induced motions, the velocities are plotted in Figure 9 at different times. Compared to the case with wall-induced motions shown in Figure 8, the velocities are completely different. Without the wall-induced motions, the profiles are qualitatively more similar to the case with large aspect ratio, $r = 30$ in Figure 4. This implies that the wall-induced motions are critical when the aspect ratio is not significantly large.

To illustrate the effects of wall-induced motions, the concentration disturbances of two cases are displayed in Figure 10, in which

$$\alpha^+ = \frac{1}{\pi}\int_0^{\phi_1} \Psi d\phi - \frac{1}{2}, \alpha^- = \frac{1}{\pi}\int_{\phi_2}^{0} \Psi d\phi - \frac{1}{2} \tag{35}$$

for the case excluding wall-induced motions and α_w^+ and α_w^- are for the case including them. Here, α^+ and α^- refer to the concentration disturbances of the fibers with $\phi > 0$ and $\phi < 0$, respectively. When the wall-induced motions are excluded, one can observe the accumulation of fibers with $\phi > 0$ and depletion of fibers with $\phi < 0$ according to α^+ and α^-. However, when the wall-induced motions are included, this concentration disturbance is highly reduced. Moreover, the gradient of the concentration is smaller. Thus, diffusion does not play the same major role here. This change is due to the wall-induced "glancing" turn and "reversing" turn of the fibers.

Initially, the disturbance flow is small and the rotational motions of the fibers are dominated by $\dot{\phi}_w$. Considering a fiber settling sideways toward the wall having an angle ϕ.

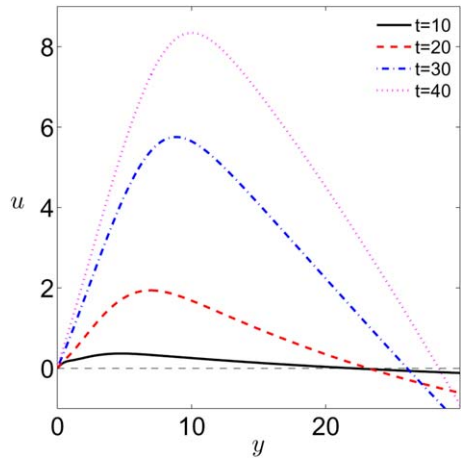

Figure 9. Aspect ratio $r = 10$.

Disturbance velocities at time $t = 10$, 20, 30, and 40 when the wall-induced motions are excluded. [Color figure can be viewed in the online issue, which is available at wileyonlinelibrary.com.]

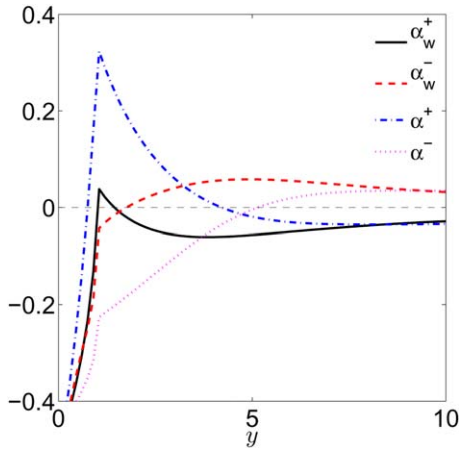

Figure 10. Aspect ratio $r = 10$ and at $t = 10$.

Concentration disturbances of the fibers with $\phi>0$ (α^+ and α_w^+) and $\phi<0$ (α^- and α_w^-), see (35). α^+ and α^- are for the case excluding wall-induced motions whereas α_w^+ and α_w^- include wall-induced motion. [Color figure can be viewed in the online issue, which is available at wileyonlinelibrary.com.]

After a close interaction with wall, for example, by the "glancing" turn or "reversing" turn, the fiber has an angle $-\phi$ and translates away from the wall with a horizontal velocity equal in magnitude but opposite to the approach velocity. The "reversing" turn is particularly clear from the flux arrows in Figure 8a. In Figure 11, f_ϕ^r is F_ϕ at $\phi=\pi/2$ and f_ϕ^g is F_ϕ at $\phi=0$. The definition of F_ϕ is given in (16). The flux f_ϕ^r refers to the flux when the fibers turn through the horizontal and f_ϕ^g refers to the flux when the fibers turn through the vertical. When $\dot{\phi}_w$ is included (Figure 11a), f_ϕ^r illustrates the significant "reversing" turn and f_ϕ^g the "glancing" turn, that is, both of them rotate fibers toward an orientation favorable for fiber settling away from the wall. Thus, the depletion of fibers initially with orientation $\phi < 0$ due to positive settling velocity is replenished by the turning of new fibers into this orientation. However, without wall-induced motions (Figure 11b), f_ϕ^g can be neglected and f_ϕ^r shows a different direction of the flux. This is due to that the rotational motions are only controlled by the shear. This would enhance the depletion of fibers near the wall, inducing a strong backflow.

Moreover, according to the nondimensional, wall-induced rotation rate of the fiber in (31) and (32), $(\dot{\phi}_0, \dot{\phi}_1) \sim \frac{f(y)}{2\ln(2r)-1}$. Thus, a fiber with smaller aspect ratio falling near a vertical wall will rotate faster. For the case with $r = 10$, fibers drifting toward the wall rotate to $\phi < 0$ rather quickly and then drift away from the wall. Hence, the deficit of fibers with $\phi < 0$ due to drift would be continuously replenished by the reversed fibers in time. For fibers with very large aspect ratio, they take longer time to rotate to $\phi < 0$. Thus, fibers approaching the wall tend to accumulate near the wall rather than turning away from it.

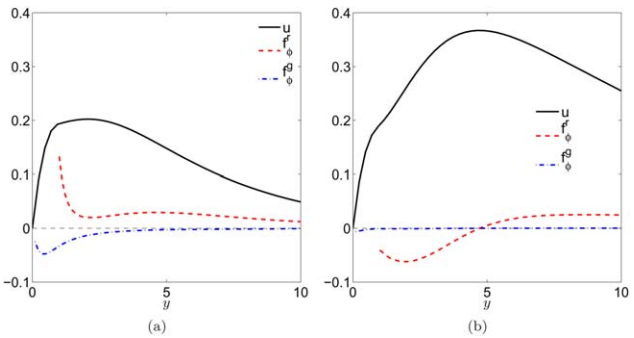

Figure 11. Aspect ratio $r = 10$ and at $t = 10$.

***u*: disturbance velocity; f_ϕ^r: orientational flux when the fibers turn through the horizontal; f_ϕ^g: orientational flux when the fibers turn through the vertical. Wall-induced motions are (a) included and (b) excluded. [Color figure can be viewed in the online issue, which is available at wileyonlinelibrary.com.]**

By realizing this, here we also do the flux analysis at $t = 10$ for the case with $r = 10$. For fibers with $\phi > 0$ (Figure 12a), the convection flux and diffusion flux are smaller than the fluxes of the case with $r = 30$ (Figure 6a). For fibers with $\phi < 0$ (Figure 12b), the convection flux is inceased next to the steric-depleted layer as compared to the case $r = 30$. These differences are due to the replenishing of fibers from $\phi > 0$ to $\phi < 0$, that is, wall-induced motions of fibers. Moreover, the range of influence of the diffusion flux is decreased. In Figure 12c, the total flux is positive near the wall, instead of negative in Figure 6c. According to the gradient of the flux, the concentration is decreased in the vicinity of the wall but increased outside, as shown by α'. This is also different from the case when $r = 30$. For fibers with $r = 10$, the depletion near the wall is weaker, including both the intensity and range of the decrease. Thus, the near-wall backflow is correspondingly weaker. Moreover, the outside fiber-rich region weakens the backflow further. With time increasing, the fiber-rich region drives a downward flow which drags the near-wall backflow downward. Eventually, the backflow vanishes whereas the near-wall depletion still exists. When the aspect ratio of the fibers is larger, $r = 30$, the replenishing of fibers is weaker, resulting in a stronger depletion near the wall. Thus, a backflow develops continuously. Meantime, the accumulation of fibers outside the near-wall depletion is also weaker and not enough to generate downward flow to drag the near-wall backflow down. As a result, a backflow grows near the wall for the case with $r = 30$.

Effects of steric-depleted boundary condition

One could also speculate that the fiber concentration deficit due to steric exclusion would create an upward flow near the wall and the shear would then reorient the fibers in such a way that they settle away from the wall. Therefore, the steric exclusion regions provide a seed for the development of the concentration instability. However, Figure 5 shows that the near-wall backflow in the beginning can be observed even without steric-depleted layer. Thus, the concentration deficit due to steric exclusion is not the origin of the instability.

To understand the effects of steric-depleted boundary condition, the velocity profiles from four cases are displayed in Figure 13, the solid line is the disturbance velocity of a homogeneous suspension but with steric-depleted layer, that is, the velocity solely driven by steric-depleted layer of the initial condition. The dash-dot line is the velocity of the case shown in Figure 5a. As the momentum equation solved is linear in the velocity and the volume fraction, the velocity field is a superposition of that due to the steric-depleted initial condition of the volume fraction and that due to the departure of the volume fraction from the initial condition. The dotted line is the latter part of the velocity field, that is, the difference between the results of the second line and first line. The dashed line is the velocity of the case shown in

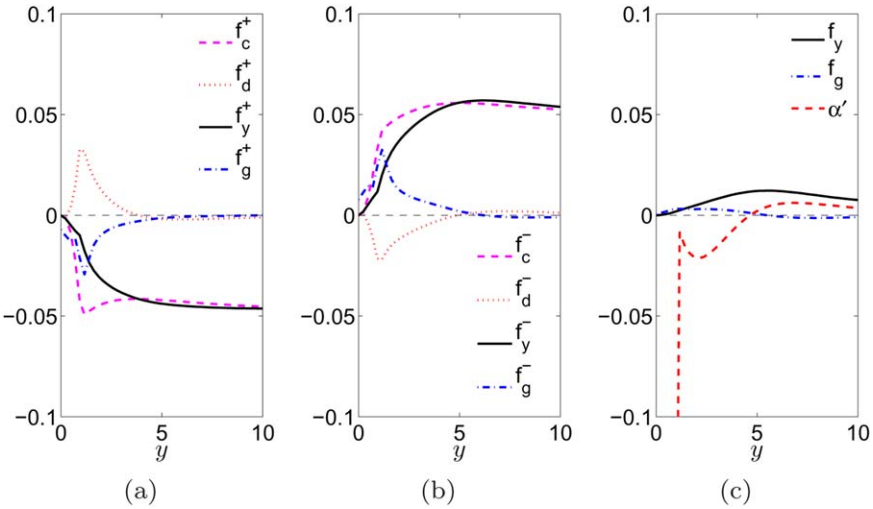

Figure 12. As for Figure 6 but with aspect ratio $r = 10$.

[Color figure can be viewed in the online issue, which is available at wileyonlinelibrary.com.]

Figure 5c, that is, the velocity field obtained using the simplified zero-flux condition, neglecting the steric-depleted layer. Thus, the volume fraction disturbance, generating the two latter, quite similar, velocity fields must be essentially independent of the velocity field at this early point of development (recall that for the case of a steric-depleted boundary condition the total velocity field is not the same as for the case of simplified boundary condition). In the very beginning, the disturbance velocity mainly consists of the steric-depleted-induced velocity. However, with time increasing, the concentration disturbance increases and the velocity becomes dominated by the concentration-disturbance-induced velocity. Subsequently, the shear of the velocity field grows large enough to influence also the orientation of the particles, and thereby, in the end, the volume fraction as a result of settling convection. The conditions are similar for the cases with $r = 10$ and smaller diffusivities.

Discussion and Conclusions

We have implemented an Eulerian approach, combined with a slender body approximation and method of images for the fibers relative motion, to investigate the convection near the sidewall in a settling fiber suspension. The results show that the near-wall convection and the mechanism of its generation are different from the intrinsic convection in the sedimentation of sphere suspensions. In sphere suspensions, the convection is due to the buoyant, steric depletion layer in the immediate neighborhood of the wall.[6] However, in fiber suspensions, the thin steric depletion layer is of secondary importance. Inhomogeneities of larger scale appear in the fiber suspension as a result of the horizontal settling component of the fibers, whose net effect for all different orientation angles is a result of the fibers hydrodynamic interaction with the wall and diffusion.

The width of the vessel is chosen to be large enough that the two sidewalls do not affect each other significantly during the simulations. In an initially quiescent and well-mixed suspension of settling fibers, the near-wall convection is always observed to be upward in the beginning, regardless of the chosen diffusivity and aspect ratio of fibers, which indicates its intrinsic nature. However, at later times, the near-wall direction of the convection depends on the aspect ratio, and also the translational diffusivity in the model.

For the case with large aspect ratio ($r = 30$ in this work), the backflow continues to grow near the sidewall, where a steric-depleted layer adjacent to the wall and an extended outer hydrodynamically depleted region are found (Figure 4). The steric-depleted layer originates from the impenetrability of a rigid fiber through a solid wall, which in sphere suspensions is the cause of the intrinsic convection. However, in fiber suspensions, a near-wall backflow is still observed even when the steric-depleted layer is eliminated artificially (Figure 5). This indicates that actually the hydrodynamically depleted region is the main cause of the near-wall backflow. In a quiescent suspension, fibers settle according to their orientation and there is also a diffusive flux when concentration gradients appear. Thus, the formation of the hydrodynamically depleted region is elucidated by a detailed analysis of this convection-diffusion

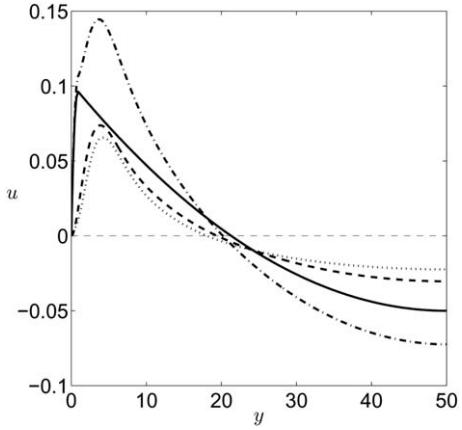

Figure 13. Aspect ratio $r = 30$ and at $t = 10$.

(–): disturbance velocity is solely driven by the steric-depleted layer of the initial condition; (− · −): disturbance velocity is calculated based on the full equations and steric-depleted boundary condition, that is, the case shown in Figure 5a; (· · ·): the difference between the results of the second line and the first line. (– –): disturbance velocity based on the full equations and no-flux boundary condition, that is, the case shown in Figure 5b.

mechanism, in which fibers are classified according to the directions they drift. It is found that the accumulation of fibers drifting toward the wall dominates in a narrow region next to the wall where the concentration is strongly increased, whereas the depletion of fibers drifting away from the wall dominates in a wider region further away from the wall where the corresponding decrease of concentration is relatively weaker (Figure 6). Thus, it is the buoyancy of this hydrodynamically depleted region which generates the backflow. Applying a smaller translational diffusivity (Figure 7), the depleted region is narrower with a weaker backflow and with time the near-wall backflow eventually disappears. Instead, a near-wall downward flow can be observed. However, when the wall-induced motions are not included in the simulations, the backflow near the wall is always obtained regardless of the diffusivities. Thus, the reason of the reversion of the near-wall convection is related to the wall-induced motions.

This is confirmed when adopting a smaller aspect ratio ($r = 10$ in this work). Due to the fiber-wall interaction, for example, by a "glancing" or "reversing" turn, a fiber drifting toward the wall is rotated into an angle for which fiber settling is away from the wall (Figure 11). Thus, the depletion of fibers initially drifting away from the wall with orientation $\phi < 0$ is replenished by the turning of new fibers into this orientation. As a result, the concentration disturbances of the two classified kinds of fibers are highly reduced and the gradients of the concentration disturbances become smaller. Therefore, the effects of diffusion are also reduced (Figure 10). Additionally, the total concentration is weakly decreased in the vicinity of the wall but increased outside owing to the turning-away fiber-wall interactions. Thus, the near-wall backflow is correspondingly weaker and the outside fiber-rich region weakens the backflow further. With time increasing, the fiber-rich region drives a downward flow which drags the near-wall flow downward. Eventually, the backflow vanishes whereas the near-wall depletion still exists (Figure 8). However, fibers falling near a sidewall with significantly large aspect ratio, rotate more slowly and consequently tend to accumulate near the wall rather than turning away from it as they approach the wall. Thereby, the convection-diffusion mechanism described above dominates the evolution at large enough aspect ratio.

We also illustrate that the steric-depleted boundary condition is not critical in the generation and evolution of the near-wall convection (Figure 13).

Finally, we address the possible extension of the model to 3-D flow applications. A difficulty arises here as the Fokker–Plank equation is formulated in both physical and orientational space. Thus, we have a time dependent problem in five dimensions. Implementing this into a commercial software is not a standard feature and the computational effort might be quite heavy if details of the flow field and fiber orientation are wanted. One way to reduce the computational effort is to reduce the problem to the standard three space dimensions by considering only a limited number of moments of the orientation distribution function in each point and time instant. Closure approximations for such structure functions, that is, the orientations tensors, are available in the literature, see for example, Advani and Tucker.[31] From the Fokker–Plank equation, a set of evolution equations can be derived for the orientation tensors, which then would be solved in parallel with the Navier–Stokes equations. An approximation to the orientation distribution can then be reconstructed from these orientation tensors. In the development of such an engineering tool, the present two-dimensional results for fibers settling next to a wall could serve as a valuable basic test case for validation purposes.

Acknowledgment

This work was supported by the China Scholarship Council (CSC) and the Swedish Research Council (VR).

Literature Cited

1. Beenakker CWJ, Mazur P. Is sedimentation container-shape dependent? *Phys Fluids*. 1985;28(11):3203–3206.
2. Geigenmüller U, Mazur P. Sedimentation of homogeneous suspensions in finite vessels. *J Stat Phys*. 1988;53(1–2):137–173.
3. Geigenmüller U, Mazur P. Intrinsic convection near a meniscus. *Phys A: Stat Mech Appl*. 1991;171(3):475–485.
4. Bruneau D, Feuillebois F, Anthore R, Hinch EJ. Intrinsic convection in a settling suspension. *Phys Fluids*. 1996;8(8):2236–2238.
5. Bruneau D, Feuillebois F, Blawzdziewicz J, Anthore R. Three-dimensional intrinsic convection in dilute and dense dispersions of settling spheres. *Phys Fluids*. 1998;10(1):55–59.
6. Peysson Y, Guazzelli É. An experimental investigation of the intrinsic convection in a sedimenting suspension. *Phys Fluids*. 1998;10(1):44–54.
7. Saintillan D, Shaqfeh ESG, Darve E. The growth of concentration fluctuations in dilute dispersions of orientable and deformable particles under sedimentation. *J Fluid Mech*. 2006;553:347–388.
8. Dahlkild A. Finite wave length selection for the linear instability of a suspension of settling spheroids. *J Fluid Mech*. 2011;689:183–202.
9. Nitsche JM, Brenner H. On the formulation of boundary conditions for rigid nonspherical Brownian particles near solid walls: applications to orientation-specific reactions with immobilized enzymes. *J Colloid Interface Sci*. 1990;138(1):21–41.
10. Nitsche JM. Hydrodynamic coupling and non-equilibrium distribution in pore diffusion of nonspherical fine particles. *Part Sci Technol*. 1991;9(3–4):135–148.
11. Schiek RL, Shaqfeh ESG. Nonlocal theory for stress in bound, Brownian suspensions of slender, rigid fibres. *J Fluid Mech*. 1995;296:271–324.
12. Krochak PJ, Olson JA, Martinez DM. Near-wall estimates of the concentration and orientation distribution of a semi-dilute rigid fibre suspension in poiseuille flow. *J Fluid Mech*. 2010;653:431–462.
13. Caswell B. The stability of particle motion near a wall in Newtonian and non-Newtonian fluids. *Chem Eng Sci*. 1972;27(2):373–389.
14. Russel WB, Hinch EJ, Leal LG, Tieffenbruck G. Rods falling near a vertical wall. *J Fluid Mech*. 1977;83(2):273–287.
15. de Mestre NJ. Low-Reynolds-number fall of slender cylinders near boundaries. *J Fluid Mech*. 1973;58(4):641–656.
16. de Mestre NJ, Russel WB. Low-Reynolds-number translation of a slender cylinder near a plane wall. *J Eng Math*. 1975;9(2):81–91.
17. Liu H, Bau HH, Hu H. On the translation of a cylinder in a long tube. *Phys Fluids*. 2004;16:998.
18. Swaminathan TN, Mukundakrishnan K, Hu HH. Sedimentation of an ellipsoid inside an infinitely long tube at low and intermediate Reynolds numbers. *J Fluid Mech*. 2006;551:357–386.
19. Koch DL, Shaqfeh ESG. The instability of a dispersion of sedimenting spheroids. *J Fluid Mech*. 1989;209:521–542.
20. Zhang F, Dahlkild A, Lundell F. Nonlinear disturbance growth during sedimentation in dilute fibre suspensions. *J Fluid Mech*. 2013;719:268–294.
21. Jeffery GB. The motion of ellipsoidal particles immersed in a viscous fluid. *Proc R Soc London Ser A*. 1922;102:161–179.
22. Batchelor GK. Slender-body theory for particles of arbitrary cross-section in stokes flow. *J Fluid Mech*. 1970;44(3):419–440.
23. Keller JB, Rubinow SI. Slender-body theory for slow viscous flow. *J Fluid Mech*. 1976;75:705–714.
24. Johnson RE. An improved slender-body theory for Stokes flow. *J Fluid Mech*. 1980;99(2):411–431.
25. Götz T. *Interactions of Fibers and Flow: Asymptotics, Theory and Numerics*. Ph.D. Thesis. Germany: University of Kaiserslautern, 2000.
26. Tornberg AK, Gustavsson K. A numerical method for simulations of rigid fiber suspensions. *J Comput Phys*. 2006;215(1):172–196.

27. Gustavsson K, Tornberg AK. Gravity induced sedimentation of slender fibers. *Phys Fluids*. 2009;21:123301.
28. Blake JR. A note on the image system for a stokeslet in a no-slip boundary. *Proc Camb Philos Soc*. 1971;70:303–310.
29. Pozrikidis C. *Boundary Integral and Singularity Methods for Linearized Viscous Flow*. Cambridge University Press, Cambridge, UK, 2005.
30. Guazzelli É, Hinch J. Fluctuations and instability in sedimentation. *Annu Rev Fluid Mech*. 2011;43(1):97–116.
31. Advani SG, Tucker CL. Closure approximations for three-dimensional structure tensors. *J Rheol*. 1990;34(3):367–386.

Manuscript received Jan. 22, 2014, and revision received Aug. 4, 2014.